RSC Advances

RSC Publishing

PAPER

Interplay of formation kinetics for highly oriented and mesostructured silicate–surfactant films at the air–water interface†

Cite this: *RSC Advances*, 2013, **3**, 3270

Ying-Huang Lai,*[ab] Siang-Wei Cheng,[b] Shiaw-Woei Chen,[b] Je-Wei Chang,[b] Chun-Jen Su,[a] An-Chung Su,[c] Hwo-Shuenn Sheu,[a] Chung-Yuan Mou[d] and U-Ser Jeng*[ac]

Received 13th November 2012,
Accepted 20th December 2012

DOI: 10.1039/c2ra22887d

www.rsc.org/advances

Kinetic details of mesostructured silicate–surfactant films formed at the air–water interface of acidic solutions of cetyltrimethylammoium bromide and tetraethyl orthosilicate were systematically studied. Time-resolved grazing-incident small-angle X-ray scattering was adopted to capture the formation kinetics of the free-standing films comprising mesostructured silicate channel domains highly oriented to the air–water interface. Evolutions of the ordered domain size and phase volume are interpreted on the basis of the Avrami analysis, from which intermediate phases and corresponding phase transitions (as modulated by temperature, pH level, and/or composition) during film formation were quantitatively identified. Extracted kinetic parameters, complemented with the rate constant of silicate hydrolysis obtained *via* Raman spectroscopy, revealed details of the dynamic interplay between silicate polymerization and inorganic–organic self-assembling. Effects of the air–water interface on the formation of the silicate–surfactant films were illustrated in terms of the highly oriented mesostructure, the greatly enhanced kinetics characterized by sporadic nucleation and diffusion-controlled growth, and the reduced activation energy for silicate polymerization, in sharp contrast to solutions without the air–water interface. A schematic diagram of the free energy *vs.* surfactant headgroup area is constructed to correlate the observed kinetics pathways for mesostructure formation during film fabrication at the air–water interface. Advantages of the interface coupling with either air–water or solution–substrate on film formation are discussed.

Introduction

Surfactant-templated silica films synthesized at the air–water interface were first demonstrated by Yang *et al.*[1] These films exhibited features of highly oriented domains of nanochanneled silica, good film flexibility, and small film roughness originated from the gravity-leveled air–water interface.[1] Thus synthesized free-standing films are readily transferable to designated substrates for various applications.[1–3] Recent developments include the syntheses of metal–copolymer films[4] and bridged amine-functionalized films[5] *via* this route. However, the current mechanistic understanding on the formation of inorganic–organic films at the air–water interface is based mostly on after-the-fact observations.[1,2,6] The understanding of the film growth mechanism and kinetics for better strategic controls of mesostructured film formation was especially emphasized by Jung *et al.*[7] Kinetic information is also desired to better understand the very recent syntheses of mesoporous silica films with vertical channels on the substrate.[8–10]

The general formation mechanism of mesostructured inorganic–surfactant assemblies was, however, proposed sometime ago,[11] which involves the parallel or sequential processes of (*i*) formation of silicate–surfactant interfaces, (*ii*) self-assembly of lyotropic phases, (*iii*) formation of a polysilicate structure, and (*iv*) phase separation of the organic–inorganic self-assemblies from the bulk solution.[11] A considerable amount of experimental observations on mesostructured silicate–surfactant films were qualitatively attributed to various combinations of these processes;[1–15] nevertheless, concomitant processes require structural formation kinetics to better assess the interplay and individual influence on the intermediate structures or kinetic pathways of the film formation.[15b]

[a]*National Synchrotron Radiation Research Center, Hsinchu Science Park, Hsinchu 30076, Taiwan. E-mail: usjeng@nsrrc.org.tw; Fax: +886-3-578-3813; Tel: +886-3-578-0281*
[b]*Department of Chemistry, Tunghai University, Taichung 407, Taiwan. E-mail: yhlai@thu.edu.tw; Fax: 886 4 23590246; Tel: 886 4 23590248*
[c]*Department of Chemical Engineering, National Tsing Hua University, Hsinchu 30013, Taiwan*
[d]*Department of Chemistry and Center of Condensed Matter Science, National Taiwan University, Taipei 10617, Taiwan*

† Electronic supplementary information (ESI) available: *In situ* GISAXS movies, SAXS data, diagram of phase evolution. See DOI: 10.1039/c2ra22887d

In situ neutron or X-ray reflection observations from the air–water interface during the formation of mesostructured silicate films were first made by Holt *et al.*[16] Grazing incidence X-ray diffraction was subsequently adopted to reveal details of the formation of three dimensionally (3D) structured thin films at the air–water interface.[6] In probing such free-floating films at the horizontal air–water interface with thickness in the nanometer scale, the X-ray or neutron beam must be properly bent to a shallow incident angle for an increased sampling volume and improved sensitivity,[18] which requires stringent instrumental measurements and control of the sample environment (*e.g.* water evaporation or environmental vibration). Based on *in situ* observations of a lamellar phase and 2D-ordered arrays of silicate–surfactant cylinders at the air–water interface, together with the correlated micelle structures revealed *via* small-angle X-ray and neutron scattering (SAXS and SANS), Edler *et al.* were able to propose a hybrid growth mechanism of micelle layering and liquid–liquid phase separation of pre-organized arrays.[6,16,17] In particular, low humidity was found to accelerate dramatically silicate–surfactant film formation.[19] Controlling the solvent evaporation of a silicate–surfactant solution was keenly developed into evaporation-induced (or accelerated) self-assembly (EISA) on solid substrates.[12,13] As EISA films are formed under far-from-equilibrium conditions, the formation mechanism leans even more sensitively on the dynamic interplay of the several interacting kinetics mentioned previously during film formation.[4,13,15,17] In such a fast-evaporation process, all kinetics associated explicitly and implicitly with the solute concentrations are enhanced with different emphases along the evaporation-induced density gradient across the film depth. Consequently, kinetically trapped intermediates and stable phases often coexist.[8,13,20–22] With such *in situ* studies, a qualitative understanding of the film formation process and morphology diagram was established for EISA films.[12,13] However, for either EISA or free-standing films, quantitative kinetic aspects in the film formation are seldom addressed. These include kinetic parameters in the self-assembly of organic–inorganic interfaces and in the silicate polymerization, which are convenient keys to the precise control and understanding of the kinetic paths in the formation of inorganic–surfactant films.[14,15]

In this study, we investigate the formation kinetics of mesostructured silicate–surfactant films isothermally formed at the air–water interface, from an acidic solution containing cetyltrimethylammoium bromide (CTAB) and tetraethyl orthosilicate (TEOS). We adopt an instrument capable of conducting grazing-incidence small-angle X-ray scattering (GISAXS) from the air–water interface,[18,23,24] with improved sensitivity for films of only a few nanometers thickness. This allows us to trace the film development at the air–water interface from the initial silicate–surfactant monolayers to the final 3D mesostructured freestanding film. The structural evolution observed *via* time-resolved GISAXS is characterized by the Avrami analysis for film formation kinetics.[14,15,25] With systematic changes in temperature, acidic level, and/or CTAB/TEOS ratio, we elucidate the collaboration and competition of the self-assembly of the inorganic–surfactant interfaces and silicate polymerization. Complementarily, the hydrolysis kinetics of the silicate source are revealed using *in situ* Raman spectroscopy. Kinetics parameters are shown to be particularly helpful in the differentiation of mixing phases from phase transitions; and the activation energy for silica polymerization is determined *via* the temperature dependence of the rate constants.[25] Three different film formation routes are identified, involving nematic (N) or lamellar (L) intermediates prior to the final 2D hexagonal (H) order, illustrating the interplay between silicate–organic self-assembly and silicate polymerization. For comparison, the kinetics for forming silicate–CTAB arrays in similar sample solutions without the air–water interface are also examined using SAXS. The pivoting role of the air–water interface on film formation is manifested in the highly orientated mesostructured domains, the drastically enhanced film formation rate, and the significantly lowered activation energy of silicate polymerization. To rationalize the observed kinetics of the structural ordering at the air–water interface, a schematic diagram of the free energy landscape *vs.* surfactant headgroup area is constructed, with the inclusion of an interface–film coupling.

Materials and methods

A series of sample solutions were prepared on the basis of a reference composition in the molar ratios of H_2O/HCl/CTAB/TEOS = 100/2/0.11/0.16. At this composition, the CTAB/Si molar ratio is *ca.* 0.69, for which 2D hexagonal (H) packing of cylindrical micelles is thermodynamically favored.[22] Sample solutions were respectively filled into a Teflon trough, 80×80 mm^2 in area and 0.7 mm in depth. The trough was further enclosed in an air-tight Al chamber for minimized water evaporation during isothermal annealing (temperature fluctuations within 0.1 °C) under approximately saturated humidity.

GISAXS from the air–water interface and transmission SAXS were conducted with the BL23A SWAXS instrument of the National Synchrotron Radiation Research Center.[18] With a 10 keV (wavelength λ = 1.24 Å) beam of 0.15 mm diameter and 0.15° incidence angle (slightly above the critical total reflection angle of ~0.12° for water), the beam could have a reasonable penetration *ca.* 1 μm in thickness for CTAB-templated silicate films. With a sample-to-detector distance of 1.37 m (vacuumed) and a 2D gas detector (200 × 200 mm^2; a linear-proportional counter of Gabriel type),[18b] GISAXS patterns were collected at 1 or 2 frames min^{-1}. Water evaporation was found to cause a lowered (0.2 μm min^{-1}) specimen position during measurements; this was compensated by periodic readjustments of the specimen position. With 14 keV X-rays and a sample-to-detector distance of 2.3 m, the transmission-type of SAXS was conducted for similar sample solutions sealed in a sample cell without the air–water interface; thin Kapton windows were used for the cell with a 5 mm X-ray path-length.

SAXS data were collected using a MAR165 CCD area detector at 1 frame per min; SAXS profiles $I(q)$ were circularly averaged from the 2D patterns as a function of $q = 4\pi\lambda^{-1}\sin\theta$ (with scattering angle 2θ) and corrected rigorously following standard procedures.[18b] Time-resolved Raman spectra were recorded for similar sample solutions as those used in X-ray scattering using a Raman spectrometer of the Dimension-Series of Lambda Solutions Incorporation, equipped with a 30 mW laser (632.8 nm in wavelength).

Avrami analysis of GISAXS data

Formation kinetics of an ordered phase after induction time t_0 are characterized by the evolution of the ordered phase volume (normalized by the maximum),

$$\alpha(t) = 1 - \exp[-K(t - t_0)^n] \quad (1)$$

where Avrami parameters K and n are related to the nucleation type and the growth mechanism.[25–29] In our case, $\alpha(t)$ is obtained from the integrated intensity $I(t)$ (normalized by its maximum) for a specific time-resolved GISAXS reflection of the silicate–CTAB film. In the Sharp–Hancock (SH) presentation[27]

$$\ln[\ln(1 - \alpha)^{-1}] = n \ln(t - t_0) + \ln K \quad (2)$$

where K and n can be conveniently extracted from the liner relationship of $\ln[\ln(1 - \alpha)^{-1}]$ *vs.* $\ln(t - t_0)$.[25–29]

Kinetics of TEOS Hydrolysis.

Analysis of Raman spectra followed that given by Baccile *et al.*[14] An overall hydrolysis rate constant k_H was used to characterize the reaction

$$\equiv\text{Si–OEt} + \text{H}_2\text{O} \xrightarrow{k_H} \equiv\text{Si–OH} + \text{EtOH} \quad (3)$$

with the corresponding rate expressed as

$$\text{d[Si–OEt]/d}t = -k_H\,[\text{Si–OEt}]\,[\text{H}_2\text{O}] \quad (4)$$

For an approximately constant water concentration $[H_2O]$ ($\approx$55.6 M) throughout the reaction, the integration of eqn (4) leads to

$$[\text{Si–OEt}]_t = [\text{Si–OEt}]_0 \exp(-k_H[\text{H}_2\text{O}]t) \quad (5)$$

With the conservation relation $[\text{Si–OEt}]_t = 4[\text{TEOS}]_0 - [\text{EtOH}]_t$, eqn (5) may be converted to

$$\ln\{1 - [\text{EtOH}]_t/[\text{EtOH}]_{max}\} = -k_A\,(t - t_o) \quad (6)$$

where the apparent rate constant k_A can be extracted by plotting $\ln\{1 - [\text{EtOH}]_t/[\text{EtOH}]_{max}\}$ *vs.* $t - t_0$, with the hydrolysis rate constant $k_H = k_A/[H_2O]$. The time-dependent $[\text{EtOH}]_t$, normalized by its maximum $[\text{EtOH}]_{max}$, was determined from the integrated intensity of the characteristic C–C–O deformation band of EtOH at 885 cm^{-1} in the *in situ* measured Raman spectra.[14,30]

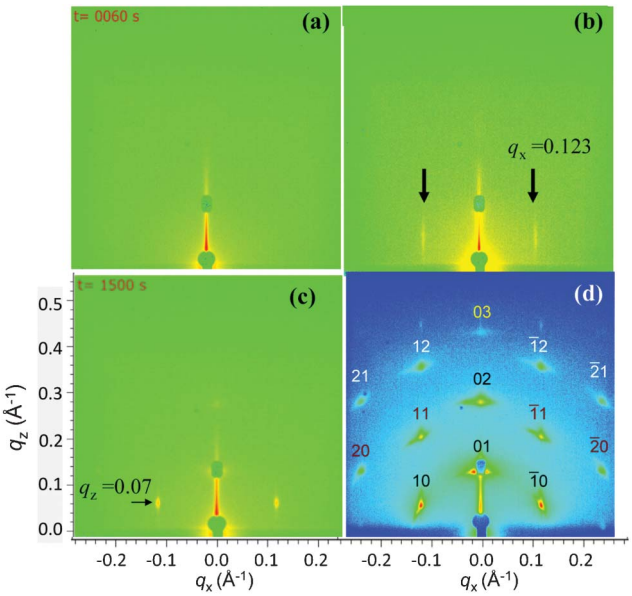

Fig. 1 Representative GISAXS patterns collected at 35 °C during the formation of a silicate–CTAB film at the air–water interface: (a) the beginning (t = 0) with a featureless image, (b) the emergence of a rod-like scattering (indicated by the arrows) at $t \approx$ 1300 s, (c) quickly sharpened reflection spots at $t \approx$ 1500 s, and (d) the fine reflections for the matured film of 2D hexagonal packing.

Results

Film formation at the air–water interface

Fig. 1 shows representative 2D GISAXS patterns collected at 35 °C during the formation of a silicate–CTAB film at the air–water interface (*cf.* movie "Route-A" in Supporting Information, ESI†). The GISAXS patterns collected in the induction period (up to $t \approx$ 1200 s) were featureless (Fig. 1a). At $t \approx$ 1300 s, a pair of faint streaks (Fig. 1b) emerged at $q_x = \pm 0.123$ Å^{-1}, indicating the formation of micellar monolayers[23,31] with a mean in-plane spacing of 5.1 nm. The streaks quickly shrank in the depth direction and developed into fine spots with $|q| = 0.141$ Å^{-1} (Fig. 1c) for a characteristic 2D hexagonal (H) packing with lattice parameter $a = 2\pi/|q| = 4.46$ nm. Fig. 1d shows the GISAXS pattern beyond $t \approx$ 10 000 s, where the reflection spots are fully indexed according to the H lattice, indicating extensively developed domains of close-packed silicate–surfactant channels oriented parallel to the air–water interface. The matured film was further scanned by GISAXS with the film laterally translated by $\pm$20 mm or in-plane rotated by $\pm 10^\circ$ with respect to the beam incidence (note that the sample dimension along the X-ray beam 80 mm was fully illuminated by the grazing incident X-ray beam); these resulted in similar GISAXS patterns, confirming the large-scale development of a mesostructured silicate–CTAB film comprising domains of hexagonally packed silicate–surfactant cylinders lying parallel to the air–water interface, although these domains are random in the in-plane orientation (*cf.* TEM images in Fig. S1, ESI†).

For a more detailed analysis, Fig. 2a gives the first few out-of-plane GISAXS profiles extracted along the streaking direc-

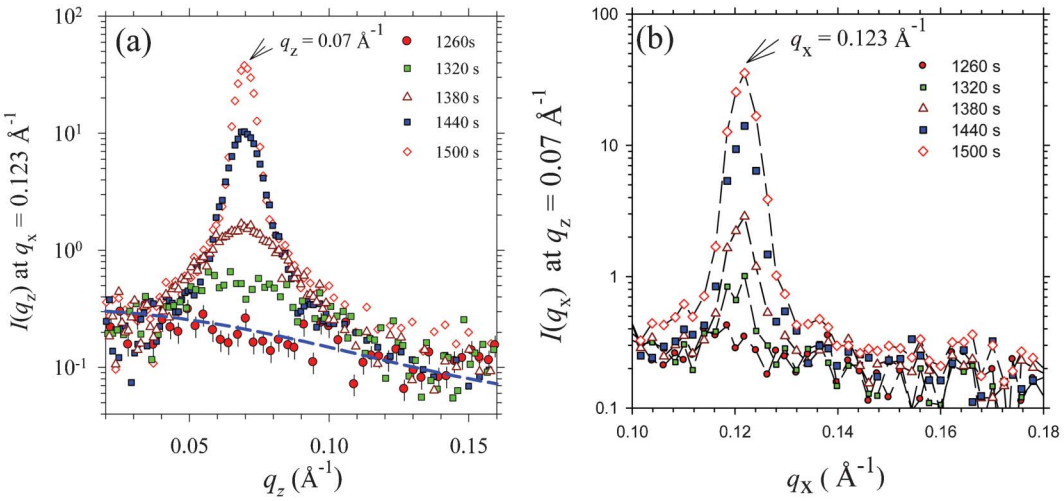

Fig. 2 Evolutions of (a) out-of-plane GISAXS profiles at q_x = 0.123 Å^{-1} (*cf.* Fig. 1b) and (b) in-plane GISAXS profiles at q_z = 0.070 Å^{-1} (*cf.* Fig. 1c) in the early stage of the film formation at 35 °C after induction time $t_o \approx$ 1200 s. The first non-trivial profile at t = 1260 s in (a) is fitted with a form factor model of core–shell ellipsoids (dashed curve). All the profiles are background-subtracted with the featureless scattering profile at t = 0.

tion at q_x = 0.123 Å^{-1} after the induction period. For the first non-trivial profile (at t = 1260 s), the data can be fitted with a model of core–shell ellipsoid form factor, with semi-major and semi-minor axes of 3.3 nm and 1.8 nm, respectively, together with a shell thickness 0.25 nm for the silica–surfactant headgroups, consistent with the core–shell micellar structure obtained using SAXS for the same solution (*cf.* Fig. S2, ESI†) or the size and shape determined *via* SANS in an earlier study[17b] of silicate–CTAB micelles. Subsequently, a halo centered at q_z = 0.067 Å^{-1} appeared, sharpened, and shifted slightly to q_z = 0.070 Å^{-1}, indicating the development of order along q_z from the surface monolayers into the bulk solution. The depth of vertical ordering, estimated from the peak width using the Scherrer equation, successively increased from 6.5 nm (1 to 2 layers) at 1320 s, to 18 nm (~4 layers) at 1380 s, to 53 nm (11 to 12 layers) at 1440 s, and to 62 nm (~14 layers) at 1500 s, considering the layer spacing of *ca.* 4.5 nm in the H phase. Correspondingly shown in Fig. 2b are the first few in-plane GISAXS profiles extracted at $q_z \approx$ 0.07 Å^{-1} and perpendicular to the rod-like scattering (*cf.* Fig. 1c). In-plane correlation lengths (as estimated from the peak width) increased concomitantly with the thickening of the surface layer, from 50 nm (1320 s), 90 nm (1380 s), 115 nm (1440 s), to 135 nm (1500 s). These results suggest that the in-plane structured monolayers of micelles deployed at the air–water interface serve as nucleation sites for the vertical growth of H domains.

Film formation kinetics

Shown in Fig. 3a are the evolutions of the integrated peak intensity $\alpha(t)$ (normalized by the maximum) for the $(10)_H$, $(20)_H$, $(11)_H$, and $(02)_H$ reflections extracted from the corresponding GISAXS patterns (*cf.* Fig. 1d). The H domain size D, extracted from the width of the (10) peak using the Scherrer equation, was found to increase with time according to $D \propto t^{0.54}$ (Fig. 3b) before saturation. As summarized in Table 1, the evolution of $\alpha(t)$ for all four representative reflections of the H phase can be fitted with the Avrami exponent n = 1.5 (±0.1), whereas values of the rate constant K generally increase with increasing temperature. The extracted Avrami exponent $n = n_N + n_G d$ consists of contributions from the primary nucleation n_N and growth $n_G d$.[26] For the former, n_N = 0 corresponds to instantaneous nucleation and n_N = 1 to sporadic nucleation; for the later, the Euclidean dimension d is between 1 and 3 and the growth type n_G = 0, 0.5 or 1 is for zero, diffusion-controlled, or phase boundary-controlled growth.[26–29] As our domain size measurements are *specific in direction*, effectively d = 1. Results shown in Fig. 3b suggest diffusion-controlled growth as $D \propto t^{0.5}$, hence n_G = 0.5 along both q_x and q_z; this leaves n_N = 1.0 for the *sporadic* nucleation of H domains. Formation of the silicate–surfactant film after the induction may hence be described by sporadic nucleation and diffusion-controlled growth.

We also conducted GISAXS for the silicate–CTAB films isothermally formed at the higher temperatures of 45 and 55 °C. A similar film formation process and development of highly ordered H domains could be observed. Moreover, a consistent value of the Avrami exponent (n = 1.5 ± 0.1) could be extracted, suggesting a common growth mechanism. The deduced rate constants increased with film formation temperature (*cf.* Table 1). On the basis of the Arrhenius law,[15] a common value of activation energy E_a = 48 ± 3 kJ mol^{-1} can be extracted from the temperature dependent K values obtained (*cf.* Fig. 4), and assigned to the formation of H-mesostructured silicate–CTAB films at the air–water interface.

Interplay from silicate polymerization

Given in Fig. 5 are the representative GISAXS patterns (*cf.* movie ''Route B'', ESI†) of the silicate–CTAB film formed at 25 °C with the same solution composition. These GISAXS patterns exhibited a similar induction stage ($t_0 \approx$ 1200 s) with featureless GISAXS patterns (*cf.* Fig. 5a), followed by the anticipated appearance (Fig. 5b) of characteristic reflections of

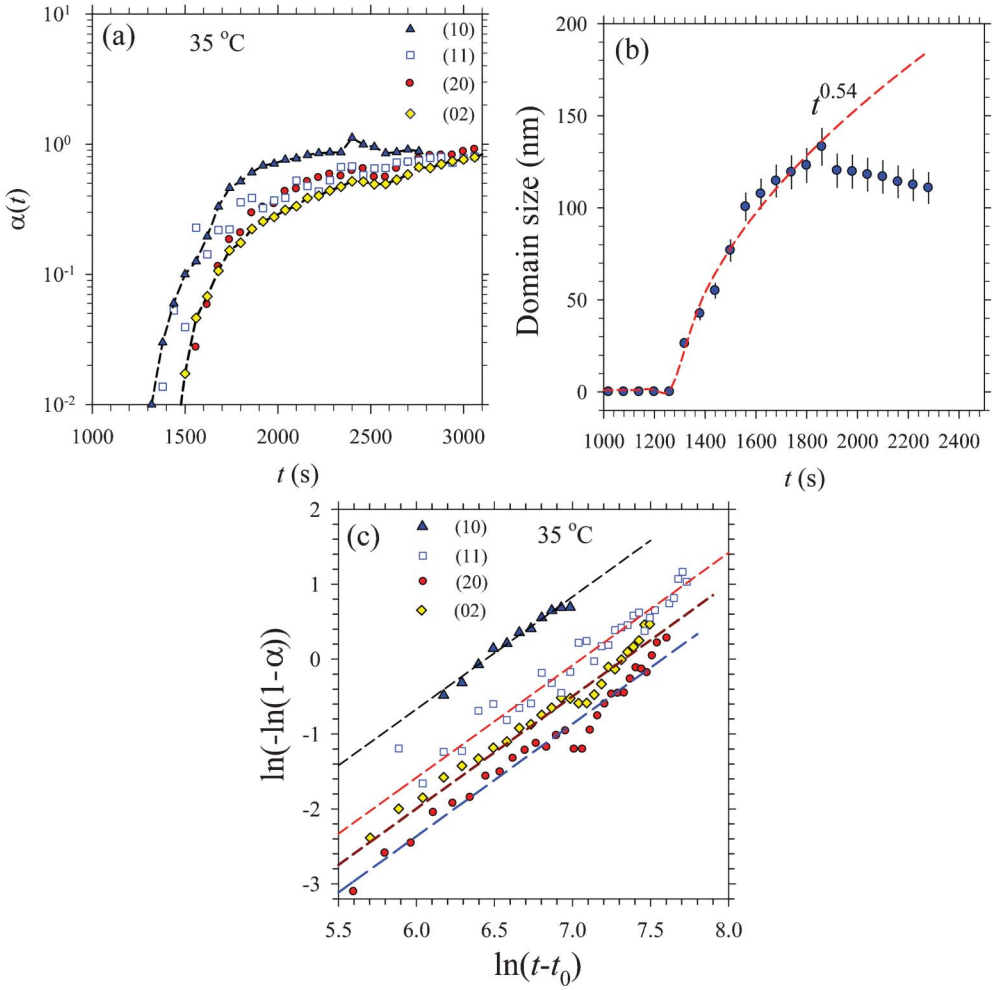

Fig. 3 (a) Evolution of $\alpha(t)$ profiles extracted from the characteristic H reflections (as indicated) of the corresponding GISAXS patterns measured for the silicate–CTAB film at 35 °C (*cf.* Fig. 1). (b) Evolution of the H domain size extracted from the profile width of (10) reflection; the size growth is fitted (dashed curve) with $D \propto t^{0.54}$. (c) Sharp–Hancock presentation for the $\alpha(t)$ profiles shown in (a) are fitted (dashed lines) with a common n = 1.5.

the L phase. The first peak (located at q_z = 0.141 Å^{-1}, *cf.* Fig. 5b) corresponded to a layer spacing of D = 4.46 nm; the characteristic (10) reflection of the H phase appeared *much later* (Fig. 5c) located at q_x = 0.1228 Å^{-1} and q_z = 0.069 Å^{-1}. With $|q|$ = 0.141 Å^{-1}, the H phase has an identical layer spacing as that for the L domains; the H lattice parameter a = $(2/\sqrt{3})$ D = 5.15 nm coincides with that observed at higher temperatures. At the late stage of film formation, the GISAXS image (Fig. 5d) exhibits the H phase reflections juxtaposed with much more prominent meridian reflections than the off-meridian ones, suggesting that a substantial amount of the L domains were kinetically trapped and unable to transform to the thermodynamically stable H phase (as also observed previously[6a]) under the critically suppressed silicate polymerization kinetics at 25 °C.

Table 1 Avrami rate constant K (in units of 10^{-5} s$^{-1.5}$) obtained for a common value of the Avrami exponent n = 1.5 ($\pm$0.1) as fitted from the representative reflections of the H phase of the silicate–CTAB nanostructure formed at the air–water interface at 25, 35, 45, or 55 °C. Note that for the 25 °C case, the values are extracted before the lamellar-to-hexagonal phase transition detailed in the text

K (10^{-5} s$^{-1.5}$)	$K(10)_H$	$K(20)_H$	$K(11)_H$	$K(02)_H$
25 °C	3.06	1.00	1.49	—
35 °C	6.32	1.68	2.54	1.59
45 °C	10.6	6.00	5.32	5.81
55 °C	18.7	8.00	6.57	7.98

The coexistence of L and H phases and transition between the two are further clarified *via* the resolution of the respective kinetic features. Shown in Fig. 6a are the evolutions of the integrated peak intensity of the representative reflections of the lamellar phase starting at $t_1 \approx$ 1260 s and that of the H phase starting at $t_2 \approx$ 2500 s. In particular, intensities of the $(10)_H$ and $(20)_H$ reflections showed concomitant enhancements at a particular time $t_3 \approx$ 4500 s (Fig. 6a); this was accompanied by intensity saturation of the meridian reflections. Since the $(1)_L$ and $(01)_H$ reflections are overlapping (due to the common layer spacing), the constant intensity (for conservation of ordered phase volume) of the meridian

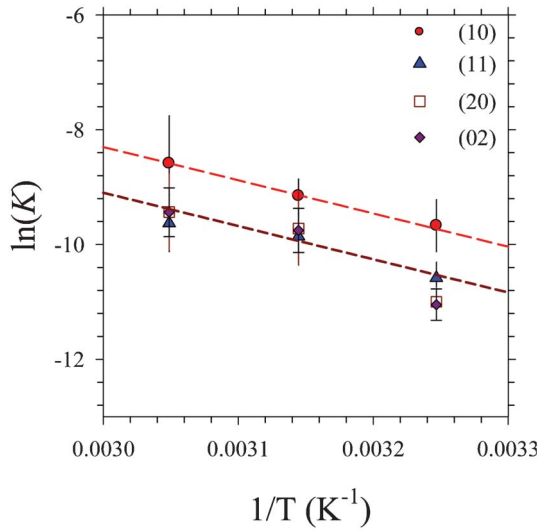

Fig. 4 Arrhenius plot of the Avrami rate constant K deduced from the intensities of $(10)_H$, $(11)_H$, $(20)_H$, and $(02)_H$ reflections of the silicate–CTAB film formed respectively at 35, 45, and 55 °C at the air–water interface. All the four sets of data are fitted (dashed lines) with the Arrhenius expression, with a common slope for the same activation energy.

reflection together with the enhanced growth of the H reflections suggest a quantitative conversion of L to H domains, *i.e.* after the transition time t_3 the further development of H domains is predominantly due to the transformation from existing L domains. Fig. 6b shows the initial growth behavior of $D \propto t^{0.5}$ for both L and H domains as calculated from the peak width. Consistent with the suggested stages in the formation of H domains, the L domain size stopped growing upon emergence of the H domains at t_2, whereas the H domain size reached a maximum at t_3 and subsequently *decreased*. This is consistent with the proposed L-to-H transformation starting at t_3: as L domains were comparatively small in size, the size of the H domains freshly converted from the pre-existing L domains should be comparable to $D_L \approx 110$ nm, smaller than that ($D_H \approx 190$ nm) of H domains at t_3. The final size of $D_H \approx 150$ nm suggests that nearly half of the final H domains were transformed from the L phase.

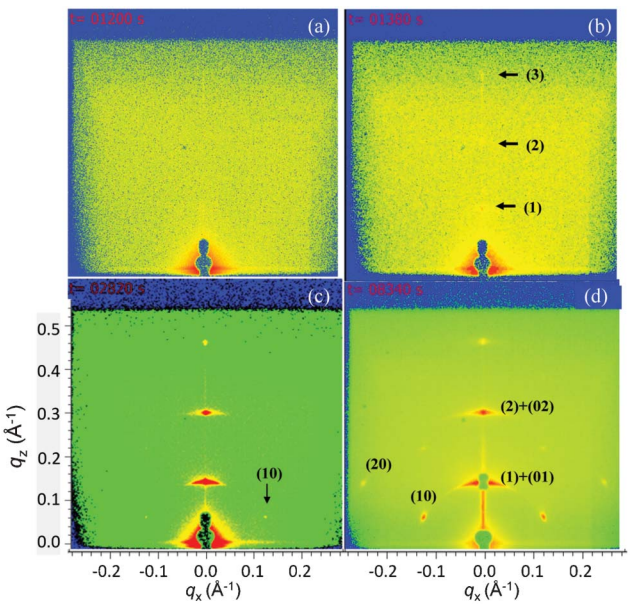

Fig. 5 Representative GISAXS patterns collected from the air–water interface during the formation of a silicate–CTAB film at 25 °C: (a) under incubation at t = 1200 s, (b) lamellar reflections at t = 1380 s, (c) weak $(10)_H$ reflection at t = 2820 s, and (d) coexisting L and H reflections at t = 8340 s, near the end of film formation.

For the H phase before the L-to-H transition, the Avrami exponent $n \approx 1.5$ extracted from the $(10)_H$ reflection (Fig. 7) is consistent with that obtained at higher temperatures. Moreover, the extracted rate constant $K = 3.06 \times 10^{-5}$ $s^{-1.5}$ (*cf.* Table 1) agrees well with the value calculated from the activation energy obtained for the H domains at higher temperatures (*cf.* Fig. 11d below). These, together with the similar growth behavior (Fig. 6b), suggest that the growth of the H domains at 25 °C in the early stage is concomitant with (but independent of) the growth of the L domains. Upon launching of the L-to-H transition at t_3, the growth mechanism of the H domains changed from n = 1.5 to n = 4 (Fig. 7), suggestive of a change in the transformation mechanism,[26–29] consistent with the proposed L-to-H transformation on the basis of decreasing H domain size beyond t_3 in Fig. 6b.

We have also done a similar Avrami analysis with the $(1)_L$ reflection. Results indicate that the L domains initially grew with n = 2.5 and $K = 2.63 \times 10^{-9}$ $s^{-2.5}$ (Fig. 7). As the L lamellae are well oriented to the air–water interface and the size grows according to $D \propto t^{0.5}$ (Fig. 6b) for 1D diffusion-controlled growth, we have n_G = 0.5 and hence n_N = 2.0 for a constantly accelerated nucleation rate, in contrast to n_N = 1 of the H phase for a fixed rate of sporadic nucleation. The constantly accelerated nucleation rate is rarely observed in phase transformation *via* pure physical processes; it is hence likely related to the condensation of silicates at the micellar outer surface, forming a shell of lower hydrophilicity and rendering the micelles more readily driven to the air–water interface (this should occur before Si-polymerization, allowing the silicate–surfactant micelles to reorganize into lyotropic-based lamellae of no observable in-plane ordering along the air–water interface). After the emergence of H domains at t_2, the formation kinetics of the L domains were slightly reduced to n = 2.1 with $K = 2.96 \times 10^{-8}$ $s^{-2.1}$ (Fig. 7); this may probably be attributed to complications arising from the spatial competition between L and H domains for nucleation or growth.

In previous studies,[3,11] the formation of the L phase and its transformation to H phase were interpreted mainly by changes in the packing parameter $g = v_0/a_0 l$ (governed by the aliphatic chain length l, the head group area a_0, and the hydrophobic volume v_0) of the surfactant of the weakly associated $S^+X^-I^+$ of the surfactant–counterion–silica interface. With the largely neutralized inorganic–organic interface and hence a decrease in a_0 from that of pure surfactant micelles, g may expectedly increase to a value greater than 1/2 for the L phase with planar interfaces. After the start of silicate polymerization, the increased charge repulsion at the inorganic–organic interface

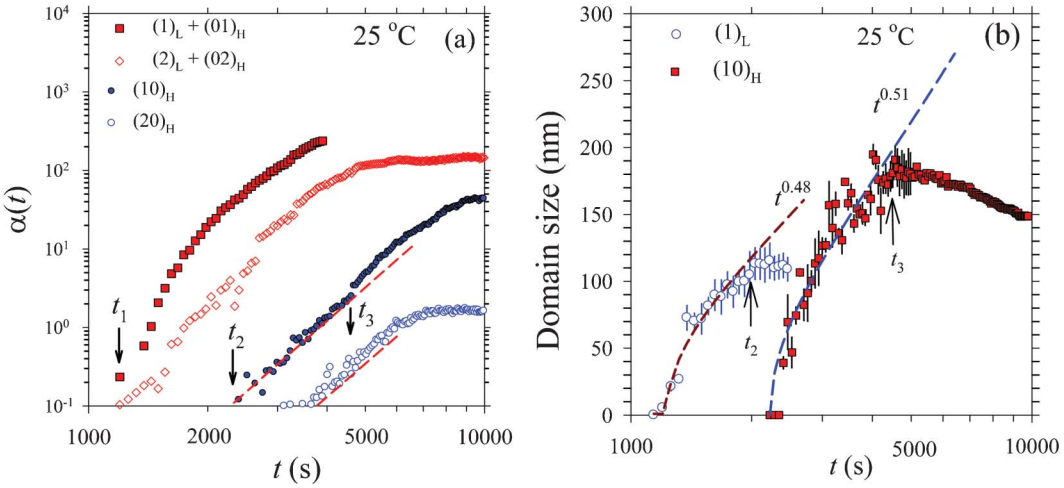

Fig. 6 (a) Evolution of the integrated peak intensity $\alpha(t)$ for the $(1)_L$, $(2)_L$, $(10)_H$, and $(20)_H$ reflections of silicate–CTAB assemblies formed at the air–water interface at 25 °C. Due to detector saturation, the strong $(1)_L$ peak in the later stage could not be traced. The arrows indicate the onset of L formation at $t_1 \approx 1260$ s, the emergence of the H phase at $t_2 \approx 2700$ s, and the L-to-H transition at $t_3 \approx 4500$ s. Dashed lines highlight the enhanced developments of $(10)_H$ and $(20)_H$ peaks after t_3. (b) Evolution of the L and H domain sizes extracted from $(1)_L$ and $(10)_H$ reflections are respectively fitted (dashed curve) with $D \propto t^{0.5}$. Note that the size growth reaches plateau/maximum at t_2 for *L* and t_3 for H domains, respectively.

leads to an increased a_0 for a smaller g value (between 1/2 and 1/3), favoring the higher curvature of the cylindrical micelles and hence the L-to-H transformation. To summarize, our kinetic results reveal a sequence of stages during film formation: nucleation-dominated and diffusion-controlled L phase formation, suppressed growth (and nucleation) of L domains upon emergence and competitive development of H domains, followed by a quantitative L-to-H transformation.

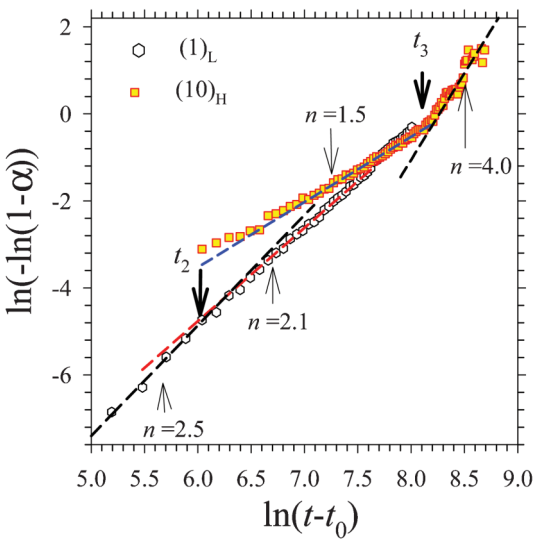

Fig. 7 Sharp–Hancock presentation of the $\alpha(t)$ profiles extracted from the $(1)_L$ and $(10)_H$ reflections of the silicate–CTAB film formed at 25 °C (*cf.* Fig. 6). The profiles are fitted (dashed lines) with the *n* values indicated. The thick arrows indicate the concomitant onsets of H domain formation and growth transition of L domains at $t_2 \approx 2500$ s, as well as the L-to-H transition at $t_3 \approx 4500$ s.

Acidity effects

It has been previously suggested[2] that a weakened association between surfactants and silicate in the acidic environment could facilitate the self-assembly of the inorganic–organic interfaces for lyotropic phases. It is also well-known that the acidic level may strongly affect the hydrolysis rate of the silicate source.[3,14,32] By changing the solution acidity, here we illustrate quantitatively the relative rate changes of both the self-assembly of the inorganic–organic interfaces and the silica polymerization on the modulation of formation pathways.

Upon a decrease in the HCl concentration, C_{HCl}, from 1.1 to 0.275 M (by a factor of 4), the induction time for the formation of silicate–CTAB self-assemblies at the air–water interface at 25 °C was dramatically prolonged, such that we had to increase the TEOS concentration by a factor of four to bring the film formation process back to the practical time scale for GISAXS measurements. Without changing the acidic level, a four-fold increase of TEOS concentration alone was found to result in the earlier appearance of the L reflections (*ca.* 60 s *vs.* 1200 s), followed by H reflections (Fig. S3, ESI† and Tables 1 and 2) prior to the L-to-H transformation. Nevertheless, the effect of the acidity reduction could override that of the enhanced TEOS concentration, leading to an extremely long induction time for the emergence of silicate–CTAB arrays at the air–water interface. As a result, a characteristically different route with an N intermediate (instead of the L phase) was observed.

Shown in Fig. 8 are the representative GISAXS patterns for the N-to-H route (with details illustrated in the movie "Route-C", ESI†). After a long induction time of $t_0 \approx 24\,600$ s, the first non-trivial GISAXS pattern (Fig. 8a) exhibited a weak broad ring centered at $q = 0.137$ Å^{-1}, revealing the formation of a nematic order by silicate–CTAB arrays of random domain orientation. The characteristic spacing of 4.59 nm extracted from the power ring position is slightly larger than the layer spacing 4.42 nm observed previously. After the appearance of

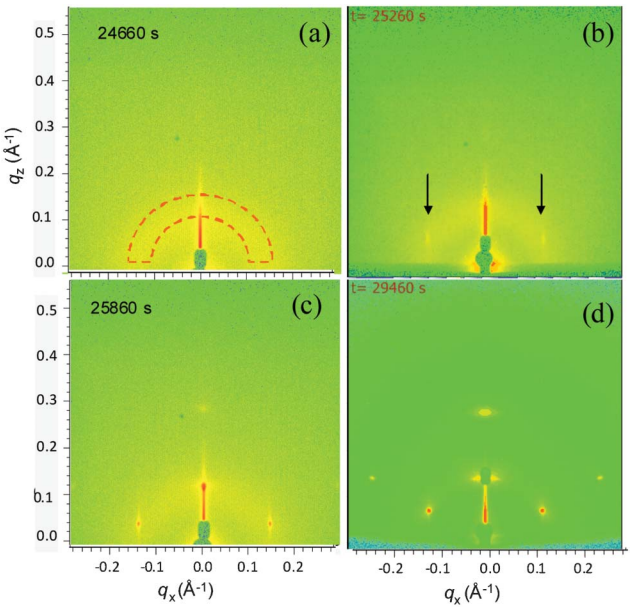

Fig. 8 Representative GISAXS patterns collected from the air–water interface of a sample solution, with increased silicate $4C_T$ but reduced acidity $1/4C_{HCl}$, at 25 °C isothermal annealing: (a) emergence of a powder ring at t = 24 660 s, after a long induction time, (b) appearance of weak streaks at t = 25 260 s, (c) prominent $(10)_H$ reflections at t = 25 860 s, and (d) H pattern at t = 29 460 s.

the nematic domains, the evolution of the GISAXS patterns followed that observed at higher temperatures for the H phase (*cf.* Fig. 1), including the rod-like scattering at $t \approx 25\,000$ s (Fig. 8b) and the gradually developed reflections for highly oriented and ordered H domains (Fig. 8c). The final GISAXS pattern (Fig. 8d) resembles that obtained at higher tempera-

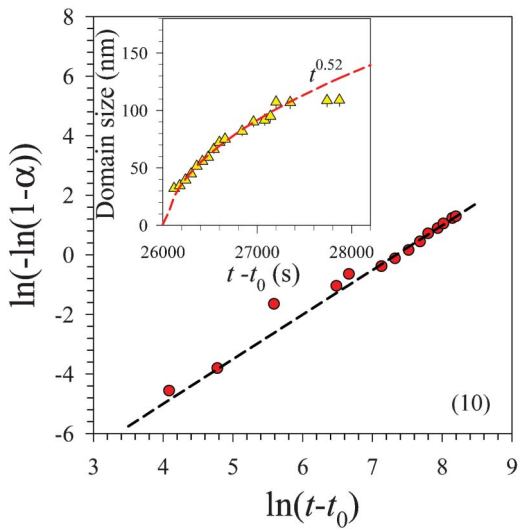

Fig. 9 Sharp–Hancock presentation of the $\alpha(t)$ profile extracted from the $(10)_H$ reflection of the silicate–CTAB film formed at 25 °C (*cf.* Fig. 6) with $C_{HCl}/4$ and $4C_T$. The profiles are fitted (dashed lines) with $n \approx 1.5$. Inset shows the corresponding domain size growth extracted from the $(10)_H$ peak width, which is fitted (dashed curve) with a power-law growth of $t^{0.52}$ as indicated.

Table 2 Avrami exponent n and rate constant K, along with the H domain emergence (induction) time t_H, obtained for the $(10)_H$ and $(11)_H$ reflections of silicate–CTAB films formed at the air–water interface from solutions of different acidic levels, C_{HCl} (1.1 M) *vs.* $C_{HCl}/4$ (0.275 M), but a common TEOS concentration of $4C_T$

	$(10)_H$		$(11)_H$	
4 C_T; 25 °C	n	K (10^{-5}s$^{-1.5}$)	n	K (10^{-5}s$^{-1.5}$)
C_{HCl} ($t_H \approx 200$ s)	1.50	14.8	1.53	7.03
$C_{HCl}/4$ ($t_H \approx 24\,600$ s)	1.50	1.67	1.52	0.79

tures (*cf.* Fig. 1) of dominated H domains, implying the complete conversion of the N phase into H domains.

Avrami analysis of the $(10)_H$ and $(11)_H$ reflections for the formation of the H phase upon change of the acidic level (Fig. 9) led to the Avrami exponent $n \approx 1.5$ (Table 2). In spite of a drastically prolonged induction, diffusion-controlled growth (*cf.* Fig. 3b and 6b) of the H domain size $D \propto t^{0.52}$ is retained (inset of Fig. 9). Nevertheless, values of the rate constant K are substantially decreased with a decreasing HCl concentration (Table 2), in clear contrast to the enhancement in K with a solely increased TEOS concentration at 25 °C (*cf.* Tables 1 and 2). It is then attempting to compensate the suppressed rate of silica polymerization due to the decreased acidic level by increasing the TEOS concentration to recover the L-to-H route which, however, was never observed. Considering the strongly extended induction time, it is most likely that the diversion from the L route to the N-to-H route is the weakened tendency toward self-assembly of the inorganic–organic interfaces upon a decreased acidic level and hence slower segregation to the air–water interface for film formation. To support this interpretation, Raman spectroscopy and SAXS evidences for self-assembly of the inorganic–organic interfaces in the bulk solution are presented below.

Hydrolysis of TEOS *vs.* condensation of silicates

Representatively shown in Fig. 10a are the time-resolved Raman spectra obtained during film formation at 25 °C. The observed marked growth of bands at *ca.* 885, 1055, and 1095 cm^{-1} may be assigned respectively to the C–C–O deformation, symmetric and asymmetric C–O stretch modes of EtOH from the hydrolysis of TEOS.[14] Neglecting kinetic complications from the multiple EtOH releasing process, the overall TEOS hydrolysis rate may be represented by the integrated intensity $\alpha_R(t)$ of the 885 cm^{-1} band (normalized by its maximum) as shown in Fig. 10b for cases of successively decreased HCl concentrations from C_{HCl} to $C_{HCl}/4$. Plots of $\ln[1 - \alpha_R(t)]$ *vs.* time (*cf.* eqn (6)) in Fig. 10c reveal decreasing values of the hydrolysis rate constant from k_A = 0.0024 to 0.0012 s^{-1} with a decreasing HCl concentration from C_{HCl} to $C_{HCl}/4$, which correspond to k_H = 0.15 to 0.065 M^{-1} h^{-1} based on a constant water concentration of 55.6 M. In contrast, the k_A values were found to be insensitive to changes in the TEOS concentration (Fig. 10d).

The results of the Raman spectroscopy indicate that the rate of hydrolysis is indeed modestly suppressed by the decrease in acidic levels. However, whether the modest decrease in k_A by a

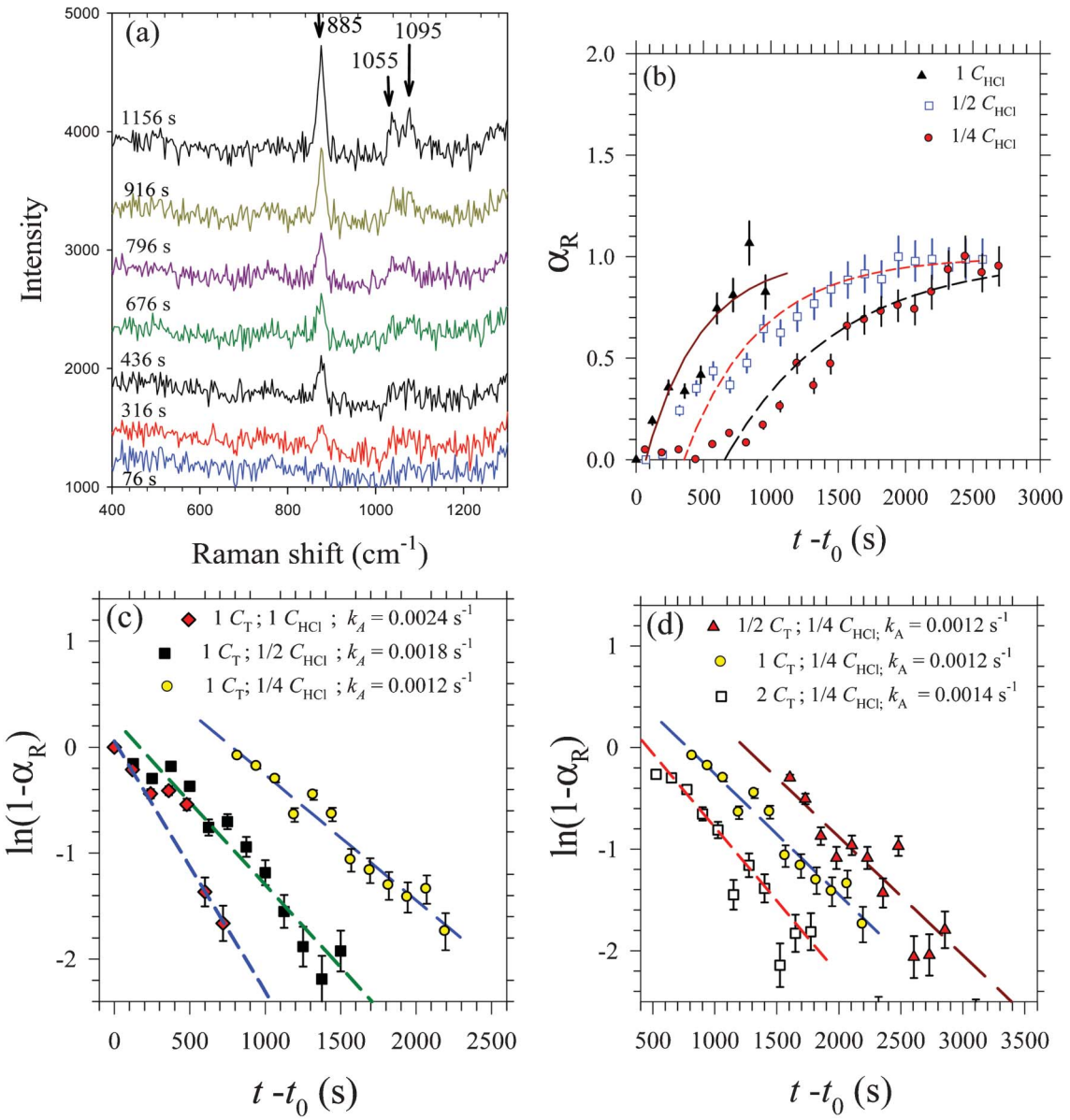

Fig. 10 (a) Time-resolved Raman spectra measured at 25 °C for solutions of systematically varied acidic levels from C_{HCl} (representatively shown), $C_{HCl}/2$, and $C_{HCl}/4$, and the reference CTAB and TEOS (C_T) concentrations. The arrows mark the characteristic bands for the stretch modes of EtOH. (b) Evolution of the integrated intensity $\alpha_R(t)$ of the 885 cm^{-1} band and (c) corresponding fitting (dashed lines, with clearly decreasing k_A values) to eqn (6). (d) Similarly fitted $\ln[1 - \alpha_R(t)]$ deduced from the Raman spectra for solutions of systematically varied TEOS concentrations from $2C_T$, C_T, to $C_T/2$, where k_A values (as indicated) are insensitive to the TEOS levels.

factor of two (Fig. 10c) was responsible for the lengthening of induction time by two orders-of-magnitude (Table 2) and the formation of the N (rather than L) intermediate, needs to be further clarified. It has been pointed out by Hench and West[30] that a decreased rate of condensation relative to that of hydrolysis may alter the silica gelation behavior from reaction-limited aggregation of compact structures to diffusion-limited aggregation of fractal-like loose structures. This suggests that diverting the L route to the N route observed with the modestly decreased acidic level may probably be related to a much more sensitively suppressed rate of silicate condensation for inorganic–organic interfaces. Indeed, previous experimental evidence[3a] has demonstrated that delayed interface neutralization allows silicate species to slowly grow and assemble with cationic surfactants, leading to a hierarchy of morphological features such as tubules-within-tubules;[3] NMR data also revealed an intimate correlation between the gelation structure (or degree of polymerization) and the silanol concentration slowly built up at the inorganic and organic interfaces.[33]

The rates of hydrolysis can be followed by *in situ* Raman spectroscopy; however, revealing the rate change in the silicate–surfactant condensation (inorganic–organic interface neutralization) requires *in situ* SAXS measurements in parallel to the study with Raman spectroscopy. Results (*cf.* Fig. S4, ESI†)

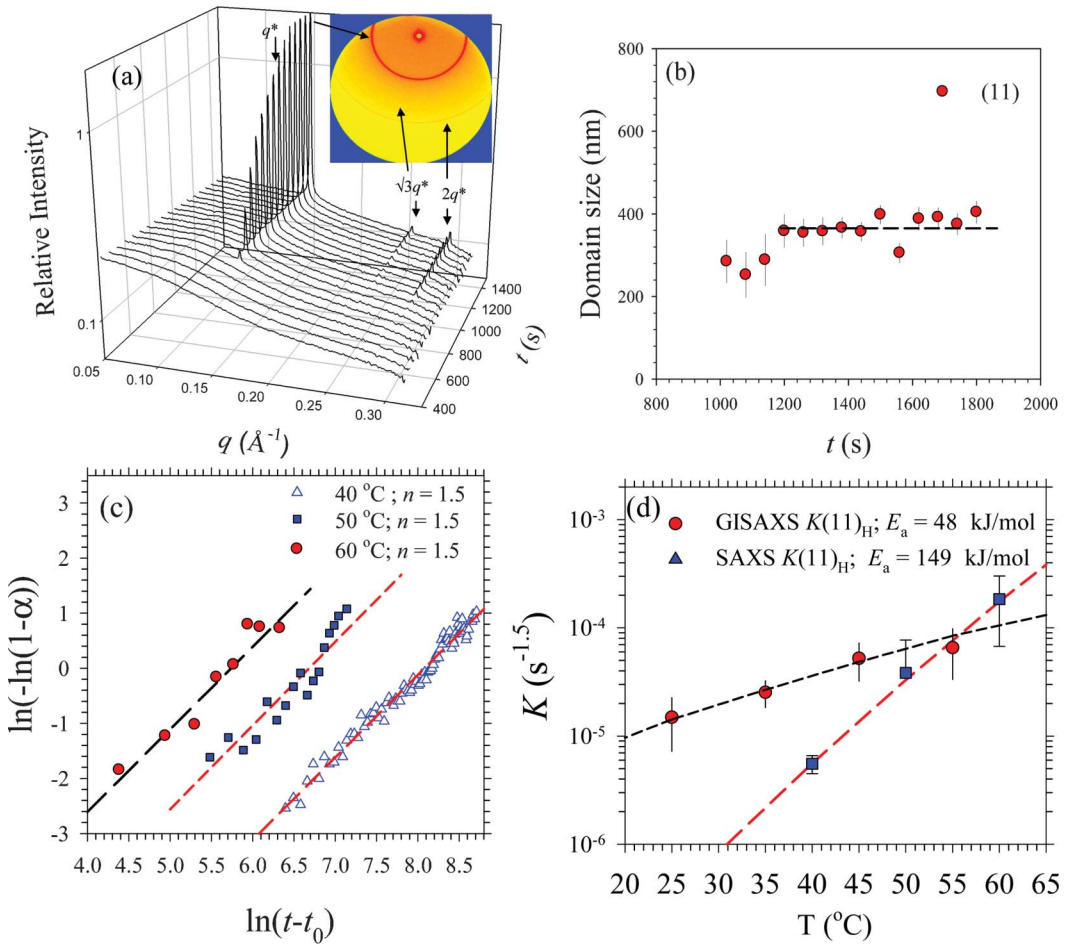

Fig. 11 (a) Representative SAXS profiles for the silicate–CTAB solution with an increased silicate concentration of $4C_T$ at 50 °C. (b) Corresponding domain size extracted from the $(11)_H$ peak using the Scherrer equation. (c) Sharp–Hancock presentation for the $\alpha(t)$ profiles extracted from the intensity evolution of the $3^{1/2}q^*$ peak in the SAXS profiles at 40, 50, and 60 °C. The data are fitted (dashed lines) with the Avrami exponent $n = 1.5$. (d) The corresponding K values are fitted with the Arrhenius equation for the activation energy E_a indicated (SAXS). For comparison, rate constants $K(11)$ for the H phase observed previously at the air–water interface (GISAXS) are also shown and similarly fitted (dotted curve).

revealed sensitive changes in the growth of zero-q intensity I_0 with decreasing acidic levels from C_{HCl} to $C_{HCl}/4$: the growth period was drastically lengthened to *ca.* 20 000 s at $C_{HCl}/4$, which was comparable to the lengthening in induction time for the structural development at the air–water interface observed *via* GISAXS (*cf.* Table 2). Note that I_0 was mainly contributed by the size of agglomerated Si–CTAB micelles,[34,35] driven by the increasingly more neutralized (hence more hydrophobic) inorganic–organic interfaces upon silicate–CTAB condensation; therefore, the much prolonged evolution of $I(q \rightarrow 0)$ (*cf.* Fig. S4d, ESI†) caused by the reduction of acidity, is indicative of a drastically decreased rate of silicate–CTAB condensation. The combination of the Raman spectroscopy and SAXS results strongly suggests that the highly asymmetric acidity effects on the rates of hydrolysis and charge condensation are responsible for the dramatically changed gelation behavior of inorganic–organic interfaces, *i.e.* from the more compact L to a more loosely arrayed N intermediate before final conversion to H domains. To lend further support to this interpretation, we examine below the formation kinetics of mesostructured silicate–CTAB arrays in bulk solutions.

Formation of silicate–CTAB arrays in bulk solutions

Time-resolved SAXS results for the sealed solutions without an air–water interface indicate the presence of randomly oriented silicate–CTAB arrays, followed by the formation of either the lamellar intermediate (d-spacing = 4.42 nm) at 25 °C (Fig. S5a, ESI†) or the H domains (a = 5.08 nm) at 45 °C (Fig. S5b, ESI†). The corresponding induction time is significantly longer, *e.g.* t_0 = 2800 s for the emergence of L domains at 25 °C in solution, compared to t_0 = 1200 s at the air–water interface. Moreover, the 2nd-order reflections of either the L or H phase tend to be much weaker than the primary reflection. With random domain orientation, the distinction between the L phase (1 : 2 : 3 in peak positions) and the H phase (of 1 : $3^{1/2}$: 2 in peak positions) relies mainly on the non-overlapping middle peak. Hence the TEOS concentration was increased to $4C_T$ and higher temperatures (40 to 60 °C) were adopted for an

enhanced intensity of this relatively weak reflection (*cf.* Fig. 11a) and appropriate measurement time range.

Fig. 11b shows the quick saturation (within the first few non-trivial SAXS profiles) of the domain size calculated from the width of the $(11)_H$ reflection (*i.e.* the $3^{1/2}q^*$ peak), in contrast to observations (*cf.* Fig. 3b, 6b, and 9) in the presence of the air–water interface. Given in Fig. 11c are the Avrami results for the integrated intensity evolutions of the $3^{1/2}q^*$ peak. Interestingly, the growth behavior is again characterized by an Avrami exponent of $n \approx 1.5$; in view of the quickly saturated domain size, the development of H domains in solution is attributed mainly to $n_N = 1.5$ for a weakly accelerated nucleation rate (presumably related to silicate polymerization). The temperature dependence of the rate constants extracted (shown in Fig. 11c) corresponds to an activation energy of E_a = 149 ($\pm$10) kJ mol^{-1}, much higher than that (48 kJ) for the H phase formation at the air–water interface.[15] Due to this stronger temperature dependence, the extrapolated rate for the formation of the H phase in bulk solution is expected to exceed that of the interfacial route above 55 °C (Fig. 11d).

It has been shown that the air–water interface[16–18] can facilitate effectively the alignment of inorganic–surfactant channel domains. The integrated SAXS and GISAXS results presented here (Fig. 11c) elucidate further the effects of the air–water interface enhancements of the kinetics aspects and the greatly reduced E_a for silicate polymerization and H domain formation; we attribute these effects to a coupling of the inorganic–organic interfaces to the air–water interface. In bulk solutions, such inorganic–organic interfaces are expected to fluctuate substantially owing to their vanishingly small interfacial tension and a small density difference across the interfaces.[36] By coupling to the stiff air–water interface with a high surface tension ($\sim$35 mN m^{-1} for the CTAB occupied air–water interface),[37] the inorganic–surfactant interfaces can be better stabilized for silicate polymerization. Consequently, the growth mechanism changes from auto accelerated nucleation ($n_N \approx 1.5$) in solution to nucleation-and-growth (n_N = 0.5 and n_G =1.0) at the air–water interface.

Coupling to the stiff air–water interface might contribute to the small surface roughness of a few angstroms reported previously for the free-standing films.[1,2] Scattering intensity from an ordered structure, especially a stratified one, is well-known to decay according to $I(q) \sim I_0(q) \exp(-q^2\xi^2)$,[36] where ξ is the root-mean-squared interface roughness. Thereby, smaller ξ for the free-standing films formed at the air–water interface can be evidenced from the less attenuated 2nd-order reflection (*ca.* 20% of the primary reflection intensity, *cf.* Fig. 1d) for the L or H domains formed at the air–water interface, compared to the highly decayed 2nd-order reflection (*ca.* 5% of the primary peak intensity, *cf.* Fig. 11a and S4). We note that the coupling effect may apply to films that are attached and grown from a solution–substrate interface as well. Previous studies[2,38] already demonstrated with TEM images that silicate–surfactant arrays coupled to the mica–solution interface exhibited fairly small layer undulations, comparable to that coupled to the air–water interface. To summarize our observations of the different routes for the formation of silicate–CTAB films consisting of H domains at the air–water interface, schematic presentations of the three kinetic paths are given in Fig. 12.

Discussion

Free energy landscapes and kinetic pathways

It has been previously proposed[11] that the free energy of a silicate–surfactant system ΔG comprises (1) ΔG_{inter} for the formation of the inorganic–organic interfaces, (2) ΔG_{org} for the organization of the inorganic–organic lyotropic phases, (3) ΔG_{inorg} for the interactions between inorganic species (includ-

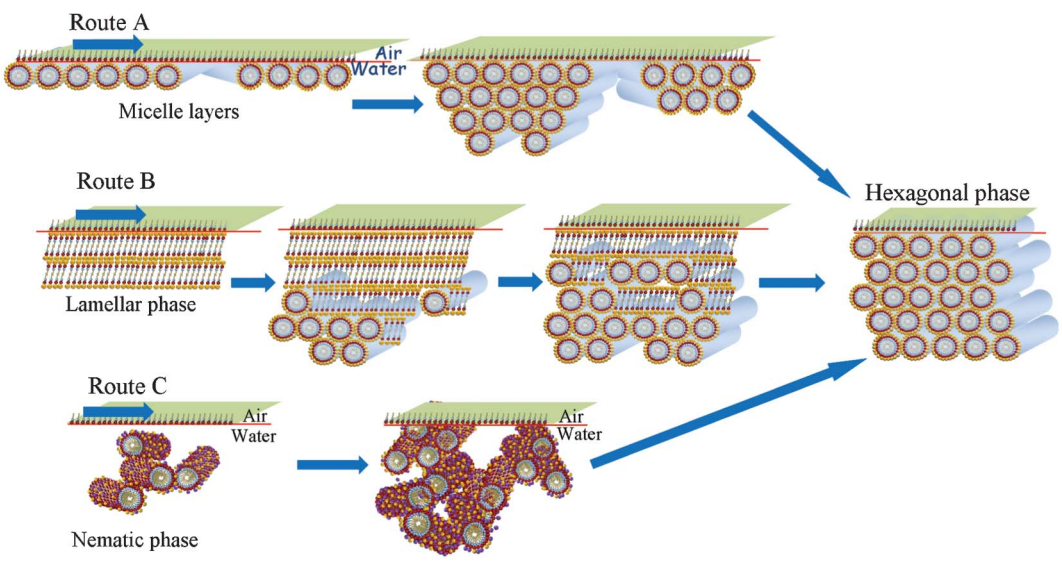

Fig. 12 Cartoons for Routes A, B, and C for the formation of silicate–CTAB films at the air–water interface, depending on the interplay of the formation kinetics and the coupling of the silicate–surfactant interfaces with the air–water interface.

ing polymerization and hydrogen bonding), and (4) ΔG_{sol} for the chemical potential of the solution phase. Modulating these relative contributions allows the selection of a particular kinetic path for mesostructure formation. For film growth attached to the air–water interface, we further propose an additional term ΔG_{sur} to the free energy

$$\Delta G = \Delta G_{inter} + \Delta G_{org} + \Delta G_{inorg} + \Delta G_{sol} + \Delta G_{sur} \quad (7)$$

to describe the observed coupling between the inorganic–organic interfaces and the air–water interface. Similar coupling was also proposed in a recent theoretical study.[39] The concept of interface coupling may also be applicable to mesostructures formed with a solution–substrate interface. Our results indicate that all terms in eqn (7) are comparable within the studied composition and temperature ranges of the silicate–CTAB system, leading to sensitive changes in the kinetics pathway by marginal changes in temperature, composition, or acidity. Our results also reveal that a lower but auto accelerating nucleation rate allows for the formation of lyotropic L domains as precursors to the thermodynamically favored H phase (*cf.* Fig. 7). Hence, it is the collective effects integrated over the entire period of structural evolution (rather than relative rates of cation–anion interface formation, organic array self-assembling, or silica polymerization at a specific point of time) that determine the kinetic path to the thermodynamically stable phase.[40]

To illustrate the integral effects of a kinetic pathway with changing rates, a free energy landscape could be helpful. As suggested in previous studies,[11] the surfactant headgroup a_0 could be used to link all terms of ΔG in eqn (7). Minimizing ΔG with respect to a_0 leads to an optimized a_0 for either a kinetically trapped intermediate phase (local minimum) or a final thermal equilibrium phase (global minimum); in other words, a_0 determines the packing parameter and hence the silica–surfactant mesostructure. Following this concept, we provide in Fig. 13 heuristic free energy landscapes that reflect the observed features of structural evolution. For mesostructure formation in bulk solution (devoid of coupling to a stiff interface, *i.e.* $\Delta G_{sur} = 0$ in eqn (7)), we would expect shallower ΔG profiles in Fig. 13, leading to lowered rates (kinetics).

Remarks on the EISA films

The different growth pathways outlined in the previous sections for the formation of silicate–surfactant arrays at the air–water interface and in solution may have implications on EISA film formation driven by the fast evaporation of solvent on a solid substrate. As the solvent quickly evaporates and the air–solvent interface vanishes, a highly oriented surface layer would form faster and joint the randomly oriented silicate–surfactant arrays underneath (in the solution) with slower kinetics; both deposit together on a bottom layer coupled to the solution–substrate interface (of enhanced formation kinetics), resulting in a largely kinetically trapped film structure with stacked multiphases or intermediates, as illustrated previously *via* TEM images and *in situ* GISAXS.[13,14] Consequently, the final structures of the EISA films (especially the interface-sandwiched zone) are highly sensitive to the initial conditions of the solution and sample enviroment.[6] In contrast, the air–water interface selects inorganic–organic interfaces with high silicate density in the formation of mesostructured free-standing films, under quasi-2D confinement. As demonstrated in this study, the final film morphology always converges to highly-oriented H domains of nearly the same lattice constant, regardless of the different formation pathways. This suggests high tolerance in the synthesis conditions for the formation of homostructured silicate–surfactant films *via* the air–water interface path.

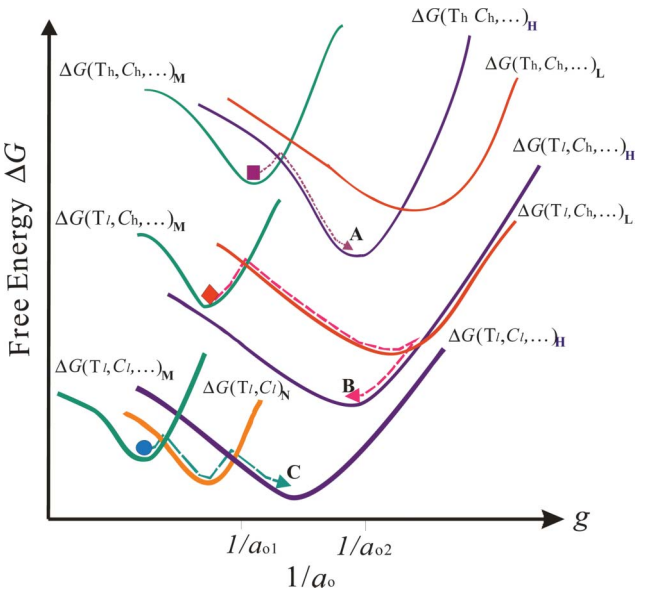

Fig. 13 Schematic free energy landscapes for the micellar phase (ΔG_M), lamellar phase (ΔG_L), nematic phase (ΔG_N), or 2D hexagonal phase (ΔG_H) of silicate–CTAB interfaces, projected onto the surfactant headgroup area a_0. Note that a_0^{-1} (a measure of surface charge density) is linearly proportional to the packing parameter g of the inorganic–organic interfaces. Different initial conditions of the micellar solution (M) are marked respectively by filled symbols (square, diamond, and circle, respectively) to indicate Routes A, B, and C (dotted paths). Starting from higher (or lower) temperatures T_h (or T_l) and higher (or lower) solute concentrations C_h (or C_l) with $\Delta G(T,C,\ldots)_M$, the free energy evolution along Route A provides a fast path to an energy minimum. Lowering the initial free energy (by a decrease in temperature) to the position marked by the diamond, we have Route B with the lamellar intermediate. A further decrease in the initial free energy (by a decrease in solute concentration) to the position marked by the circle brings about Route C with the N intermediate bridging to the global minimum of $\Delta G(T_l, C_l,\ldots)_H$. The free energy landscape ΔG_L has a local minimum with $1/a_0$ larger than $1/a_{02}$ (corresponding to g = ½), whereas ΔG_H has a minimum with $1/a_0$ situated between $1/a_{02}$ and $1/a_{01}$ (for g = ⅓). In the absence of interface coupling (*i.e.* $\Delta G_{sur} = 0$ in eqn (7)), the minimum for each free energy landscape is shifted upwards, giving a shallower profile of slower kinteics.

Conclusion

Formation kinetics of silica–surfactant mesostructures at the air–water interface and in the bulk solution of CTAB and TEOS are revealed *via in situ* GISAXS, SAXS, and Raman spectroscopy. Air–water GISAXS is particularly advantageous in resolving the highly oriented mesostructures of the free-standing films,

from which the interplay kinetics of self-assembly of the inorganic–surfactant interfaces and silicate polymerization can be distinguished. With Avrami analysis, the formation of H domains at the air–water interface is characterized by sporadic nucleation and diffusion-controlled growth. The relative rates of silicate hydrolysis, silicate–surfactant self-assembly (especially the neutralization process of the inorganic–organic interfaces), and silicate polymerization are measured and compared. Other than the obvious effect of excellent alignment of mesostructured domain, the stiff air–water interface is shown to accelerate film formation with a greatly decreased activation energy of silicate polymerization (as compared to that in the bulk solution). The kinetic information provides strategic outlines for targeting the fabrication of mesostructured silicate–surfactant films with large dimensions *via* the air–water interface, rather than the traditional bulk process.

Acknowledgements

We thank K.-F. Liao, C.-H. Su and Y.-J. Chen for assistance with GISAXS measurements. The work is supported by the National Science Council, Taiwan (Grant No. NSC 98-2113-M-029-006-MY2 and NSC 99-2112-M-213-002-MY3).

References

1 (*a*) H. Yang, N. Coombs, I. Sokolov and G. A. Ozin, *Nature*, 1996, **381**, 589–592; (*b*) H. Yang, N. Coombs and N. G. A. Ozin, *J. Mater. Chem.*, 1998, **8**, 1205–1211.
2 S. H. Tolbert, T. E. Schaffer, J. Feng, P. K. Hansma and G. D. Stucky, *Chem. Mater.*, 1997, **9**, 1962–1967.
3 (*a*) H.-P. Lin and C.-Y. Mou, *Acc. Chem. Res.*, 2002, **35**, 927–935; (*b*) H.-P. Lin and C.-Y. Mou, *Science*, 1996, **273**, 765–767.
4 (*a*) K. J. Edler, A. M. Hawley, B. M. D. O'Driscoll and R. Schweins, *Chem. Mater.*, 2010, **22**, 4579–4590; (*b*) B. Yang, R. Jaber and K. J. Edler, *Langmuir*, 2012, **28**, 8337–8347.
5 S. S. Park, J. H. Shin, D. Zhao and C. S. Ha, *J. Mater. Chem.*, 2010, **20**, 7854–7858.
6 (*a*) S. A. Holt, J. L. Ruggles, J. W. White and R. F. Garrett, *J. Phys. Chem. B*, 2002, **106**, 2330–2336; (*b*) K. J. Edler, *Soft Matter*, 2006, **2**, 284–292.
7 C. Jung, P. Schwaderer, M. Dethlefsen, R. Kohn, J. Michaelis and C. Brauchle, *Nat. Nanotechnol.*, 2011, **6**, 87–92.
8 C. Ma, L. Han, Z. Jiang, Z. Huang, J. Feng, Y. Yao and S. Che, *Chem. Mater.*, 2011, **23**, 3583–3586.
9 Z. Teng, G. Zheng, Y. Dou, W. Li, C.-Y. Mou, X. Zhang, A. M. Asiri and D. Zhao, *Angew. Chem., Int. Ed.*, 2012, **51**, 2173–2177.
10 S. Mann, *Nat. Mater.*, 2009, **8**, 781–792.
11 (*a*) A. Monnier, F. Schuth, Q. Huo, D. Kumar, D. Margolese, R. S. Maxwell, G. D. Stucky, M. Krishnamurty, P. Petroff, A. Firouzi, M. Janicke and B. F. Chmelka, *Science*, 1993, **261**, 1299–1303; (*b*) Q. Huo, D. I. Margolese, U. Ciesla, D. G. Demuth, P. Feng, T. E. Gier, P. Sieger, A. Firouzi, B. F. Chmelka, F. Schuth and G. D. Stucky, *Chem. Mater.*, 1994, **6**, 1176–1191.
12 D. A. Doshi, A. Gibaud, V. Goletto, M. Lu, H. Gerung, B. Ocko, S. M. Han and C. J. Brinker, *J. Am. Chem. Soc.*, 2003, **125**, 11646–11655.
13 (*a*) D. Grosso, F. Cagnol, G. J. de A. A. Soler-Illia, E. L. Crepaldi, H. Amenitsch, A. Brunet-Bruneau, A. Bourgeois and C. Sanchez, *Adv. Funct. Mater.*, 2004, **14**, 309–322; (*b*) F. Cagnol, D. Grosso, G. J. de A. A. Soler-Illia, E. L. Crepaldi, F. Babonneau, H. Amenitsch and C. Sanchez, *J. Mater. Chem.*, 2003, **13**, 61–66; (*c*) D. Grosso, F. Babonneau, P.-A. Albouy, H. Amenitsch, A. R. Balkenende, A. Brunet-Bruneau and J. Rivory, *Chem. Mater.*, 2002, **14**, 931–939.
14 N. Baccile, C. V. Teixeira, H. Amenitsch, F. Villain, M. Lindén and F. Babonneau, *Chem. Mater.*, 2008, **20**, 1161–1172.
15 (*a*) S. H. Tolbert, C. C. Landry, G. D. Stucky, B. F. Chmelka, P. Norby, J. C. Hanson and A. Monnier, *Chem. Mater.*, 2001, **13**, 2247–2256; (*b*) J. Patarina, B. Lebeaua and R. Zanab, *Curr. Opin. Colloid Interface Sci.*, 2002, **7**, 107–115.
16 S. A. Holt, G. J. Foran and J. W. White, *Langmuir*, 1999, **15**, 2540–2542.
17 (*a*) K. J. Edler, A. Goldar, A. V. Hughes, S. J. Roser and S. Mann, *Microporous Mesoporous Mater.*, 2001, **44–45**, 661–670; (*b*) T. Brenann, S. J. Roser, S. Mann and K. J. Edler, *Chem. Mater.*, 2002, **14**, 4292–4299.
18 (*a*) J. Als-Nielsen and D. McMorrow, *Elements of Modern X-ray Physics*, John Wiley and Sons Ltd, New York, 2001; (*b*) U. Jeng, C. H. Su, C.-J. Su, K.-F. Liao, W.-T. Chuang, Y.-H. Lai, J.-W. Chang and Y.-J. Chen, *et al.*, *J. Appl. Crystallogr.*, 2010, **43**, 110–121.
19 C. Fernandez-Martin, K. J. Edler and S. J. Roser, *Langmuir*, 2004, **20**, 10679–10684.
20 C. Yu, J. Fan, B. Tian and D. Zhao, *Chem. Mater.*, 2004, **16**, 889–898.
21 K. J. Edler, T. Brennan, S. J. Roser, S. Mann and R. M. Richardson, *Microporous Mesoporous Mater.*, 2003, **62**, 165–175.
22 (*a*) M. Matheron, T. Gacoin and J.-P. Boilot, *Soft Matter*, 2007, **3**, 223–229; (*b*) S. Besson, T. Gacoin, C. Ricolleau, C. Jacquiod and J.-P. Boilot, *J. Mater. Chem.*, 2003, **13**, 404–409.
23 G. Renaud, R. Lazzari and F. P. Leroy, *Surf. Sci. Rep.*, 2009, **64**, 255–380.
24 K. Vegso, P. Siffalovic, E. Majkova, M. Jergel, M. Benkovicova, T. Kocsis, M. Weis, S. Luby, K. Nygård and O. Konovalov, *Langmuir*, 2012, **28**, 10409–10414.
25 B. L. Kirsch, E. K. Richman, A. E. Riley and S. H. Tolbert, *J. Phys. Chem. B*, 2004, **108**, 12698–12706.
26 A. J. Müller, V. Balsamo and M. L. Arnal, *Adv. Polym. Sci.*, 2005, **190**, 1–63.
27 (*a*) M. Milanesio, G. Artioli, A. F. Gualtieri, L. Palin and C. J. Lamberti, *J. Am. Chem. Soc.*, 2003, **125**, 14549–14558; (*b*) D. Grandjean, A. M. Beale, A. V. Petukhov and B. M. Weckhuysen, *J. Am. Chem. Soc.*, 2005, **127**, 14454–14465.
28 E. Gianotti, G. Berlier, K. Costabello, S. Coluccia and F. Meneau, *Catal. Today*, 2007, **126**, 203–210.
29 M. Avrami, *J. Chem. Phys.*, 1941, **9**, 177.
30 L. L. Hench and J. K. West, *Chem. Rev.*, 1990, **90**, 33–72.
31 M. K. Bera, M. K. Sanyl, S. Pal, J. Daillant, A. Datta, G. U. Kulkarni, D. Luzet and O. Konovalov, *Europhys. Lett.*, 2007, **78**, 56003–56008.
32 C. Brinker, *J. Non-Cryst. Solids*, 1998, **100**, 31–50.

33 Q. Huo, D. I. Margolese, U. Ciesla, P. Feng, T. E. Gier, P. Sieger, R. Leon, P. M. Petroff, F. Schuth and G. D. Stucky, *Nature*, 1994, **368**, 317–321.
34 T.-L. Lin, U. Jeng, C.-S. Tsao, W.-J. Liu, T. Canteenwala and L. Y. Chiang, *J. Phys. Chem. B*, 2004, **108**, 14884–14888.
35 J.-M. Lin, T.-L. Lin, U. Jeng, Z.-H. Huan and Y.-S. Huanh, *Soft Matter*, 2009, **5**, 3913–3919.
36 U. Jeng, L. Esibov, L. Crow and A. Steyerl, *J. Phys.: Condens. Matter*, 1998, **10**, 4955–4962.
37 J. Eastoe and J. S. Dalton, *Adv. Colloid Interface Sci.*, 2000, **85**, 103–144.
38 A. Firouzi, D. Kumar, L. M. Bull, Q. Besier, P. Sieger, Q. Huo, D. Margolese, G. D. Studky and B. F. Chmelka, *Science*, 1995, **267**, 1138–1140.
39 C. Aberg, E. Sparr, K. J. Edler and H. Wennerstrom, *Langmuir*, 2009, **25**, 12177–12184.
40 P. Innocenzi, L. Malfatti, T. Kidchob, P. Falcaro, M. C. Guidi, M. Piccininic and A. Marcelli, *Chem. Commun.*, 2005, 2384–2386.